Integrated CMOS-compatible Q-switched mode-locked lasers at 1900nm with an on-chip artificial saturable absorber

Citation: Shtyrkova, Katia, et al. "Integrated CMOS-Compatible Q-Switched Mode-Locked Lasers at 1900nm with an on-Chip Artificial Saturable Absorber." Optics Express 27, 3 (February 2019): 3542 © 2019 Optical Society of America

As Published: http://dx.doi.org/10.1364/OE.27.003542

Publisher: The Optical Society

Persistent URL: https://hdl.handle.net/1721.1/124414

Version: Final published version: final published article, as it appeared in a journal, conference proceedings, or other formally published context

Research Article | Vol. 27, No. 3 | 4 Feb 2019 | OPTICS EXPRESS 3542
Optics EXPRESS

Integrated CMOS-compatible Q-switched mode-locked lasers at 1900nm with an on-chip artificial saturable absorber

KATIA SHTYRKOVA,[1,2] PATRICK T. CALLAHAN,[1] NANXI LI,[1,3] EMIR SALIH MAGDEN,[1,4] ALFONSO RUOCCO,[1] DIEDRIK VERMEULEN,[1] FRANZ X. KÄRTNER,[1,5] MICHAEL R. WATTS,[1] AND ERICH P. IPPEN[1]

[1]*Department of Electrical Engineering and Computer Science, Massachusetts Institute of Technology, 77 Massachusetts Avenue, Cambridge, MA 02139, USA*
[2]*Presently with MIT Lincoln Laboratory, 244 Wood Street, Lexington, MA 02421, USA*
[3]*John A. Paulson School of Engineering and Applied Sciences, Harvard University, 9 Oxford Street, Cambridge, MA 02138, USA*
[4]*Current address: Koç University, College of Engineering, Department of Electrical and Electronics Engineering, Rumelifeneri Yolu Sarıyer 34450 Istanbul, Turkey*
[5]*Center for Free-Electron Laser Science at Deutsches Electronen Synchrotron (DESY), Department of Physics and Center for Ultrafast Imaging, University of Hamburg, Hamburg 22761, Germany*
**katiasht@mit.edu*

Abstract: We present a CMOS-compatible, Q-switched mode-locked integrated laser operating at 1.9 µm with a compact footprint of 23.6 × 0.6 × 0.78mm. The Q-switching rate is 720 kHz, the mode-locking rate is 1.2 GHz, and the optical bandwidth is 17nm, which is sufficient to support pulses as short as 215 fs. The laser is fabricated using a silicon nitride on silicon dioxide 300-mm wafer platform, with thulium-doped Al_2O_3 glass as a gain material deposited over the silicon photonics chip. An integrated Kerr-nonlinearity-based artificial saturable absorber is implemented in silicon nitride. A broadband (over 100 nm) dispersion-compensating grating in silicon nitride provides sufficient anomalous dispersion to compensate for the normal dispersion of the other laser components, enabling femtosecond-level pulses. The laser has no off-chip components with the exception of the optical pump, allowing for easy co-integration of numerous other photonic devices such as supercontinuum generation and frequency doublers which together potentially enable fully on-chip frequency comb generation.

1. Introduction

High repetition-rate ultrafast mode-locked lasers (MLL) have unique advantages for applications such as photonic analog-to-digital converters, comb spectroscopy, optical arbitrary waveform generation and low-noise microwave synthesis. Traditionally, repetition rates beyond 1 GHz were achieved by either active modulation techniques [1,2], which restricted the pulse duration to more than a few picoseconds, with nonlinearity-induced optical bistability where multimode noise suppression was necessary for a stable operation [3,4], or by introducing a semiconductor saturable absorber, in which case the pulse duration also remained more than a few picoseconds [5–7]. Alternatively, passive mode-locking techniques have been shown to generate femtosecond-level pulses at high repetition rates when used with some form of an external repetition-rate multiplier to bring the system into the GHz-level regime [8,9]. Harmonic mode-locking, where several pulses circulate in the cavity at the same time, has also been used to demonstrate high repetition rates [10]. In all of the above cases the architecture of the laser system itself was based on a fiber laser or a diode laser, with the rest of the cavity constructed with free-space optical components. Such systems could significantly benefit from an on-chip implementation which would

#353193 https://doi.org/10.1364/OE.27.003542
Journal © 2019 Received 29 Nov 2018; revised 10 Jan 2019; accepted 10 Jan 2019; published 31 Jan 2019
Corrected: 06 February 2019

Optics EXPRESS

dramatically reduce the footprint, enable scalable mass-production, eliminate moving elements, and reduce the cost of fabrication. Moreover, the compact size of the gain cavity integrated on chip together with an on-chip passive mode-locking technique could provide GHz-level pulse repetition rates with pulse durations in the femtosecond regime without any external repetition rate multiplication [11,12]. Recent growth in integrated photonics capabilities enables such an on-chip MLL implementation in principle. Moreover, recently demonstrated wafer-scale electronic-photonic integration enables the possibility of on-chip control loops with nanosecond response time [13,14] which, when designed together with on-chip MLLs, could lead to demonstrations of fully-stabilized and fully-on-chip frequency combs and ultra-low-noise microwave oscillators.

Silicon nitride (SiN) on a silicon-on-insulator (SOI) platform is an excellent candidate for on-chip mode-locked lasers due to its low passive waveguide losses, appreciable Kerr nonlinearity, and the lack of two-photon-absorption at near infrared wavelengths [15,16]. Numerous passive photonic components necessary for integrated MLLs have already been demonstrated in this fabrication platform. These devices include wavelength filters/couplers, mode-locking elements, and integrated diffraction gratings [17,18]. The remaining challenge is an integrated electrically pumped light source, either as a continuous wavelength (CW) laser, or as a pump for an on-chip laser. One method used to achieve this involves III-V-based laser bonding to the SOI chip. More commonly an off-chip optical pump source is used for this task. For SiN on SiO_2, optically pumped gain may be incorporated on-chip, for example, in a form of a rare-earth-doped film deposited on top of the SiN/SiO_2 layers. In fact, such an approach has been successfully developed over the past 10 years [19–21], borrowing from the extensive experienced obtained with rare-earth-based fiber lasers. With a well-developed on-chip gain platform and demonstrated passive components necessary for mode-locking, it is evident that on-chip high repetition rate MLLs will follow a similar development path to that of the conventional lasers, proceeding along the path from a continuous wavelength to Q-switched, then to Q-switch-mode-locked, and ultimately to CW mode-locked devices.

The lasers in this work were developed for DARPA's Direct-On-chip-Digital-Optical Synthesizer (DODOS) program, the goal of which is to create a fully-integrated ultra-stable optical frequency synthesizer in the communications C-band, referenced to an external 10MHz clock source. MIT's approach utilizes a tunable single frequency laser that is locked to a self-referenced frequency comb, the repetition rate of which is in turn locked to the external RF source. The on-chip octave-spanning continuum generation, second-harmonic generation, and the octave-wide spectral filter required for this approach have previously been reported [22–24].

Here we describe demonstrations of compact optically pumped on-chip Q-switched and mode-locked lasers in a CMOS-compatible Si_3N_4 platform, with thulium-doped aluminum oxide glass used as a gain material. The lasers operate near 1900nm and have no off-chip components other than the optical pump source. The first demonstration of such a laser was achieved in our group in 2017 [25]. The laser had a footprint of 25 × 12 mm, cavity repetition rate of 680 MHz, a Q-switching rate of about 1 MHz, and pulse duration of 1.2 ps. In this work we demonstrate a significantly improved laser architecture that allows for truly compact devices (23.5 × 0.78 mm) and achieves a cavity repetition rate of 1.2 GHz, with bandwidth that would support 215fs pulses.

2. Laser architecture and fabrication platform

The architecture of the MLL is shown in Fig. 1. This laser consists of three gain section segments connected using compact Si_3N_4 bends. A wide photonic trench is etched in the entire gain region of the laser, shown as the shaded area in Fig. 1. The purpose of the trench is to allow the gain material deposited on top of the chip to come into close contact to Si_3N_4 layers and form the gain waveguide. This laser is pumped with an external 1614 nm L-band Erbium-doped fiber amplifier (EDFA). The pump light enters the lasing cavity via a

Optics EXPRESS

pump/signal combiner component (Section 3.1) shown in the upper left in Fig. 1. The gain waveguide consists of three nearly straight, approximately 2cm-long sections where the pump and the signal modes have large overlap with the gain material (Section 3.2). These three gain waveguide sections are connected by compact Si_3N_4 bends (Section 3.3). Prior to each bend, both the pump and the signal are transferred from a large-mode-area gain waveguide into a silicon nitride layer with a much more confined optical mode. This makes it possible to achieve tight 180-degree bends without significant losses. Following the three gain sections, the 1900nm signal is again transferred to the Si_3N_4 layer as it enters a Kerr-nonlinearity-based mode-locking element, which we refer to as a nonlinear interferometer (NLI). The NLI acts as a CW reflector for 1900nm at low incident optical power. When the incident optical power is high enough, the NLI produces intensity-dependent reflection that can increase for higher input power (Section 3.5). This produces artificial saturable absorber action and can be used to form optical pulses. The 1900nm signal is then reflected back into the laser cavity, propagates through the three gain sections, and enters the pump/signal combiner element. The pump-signal combiner is a four-port device allows most of the 1614nm pump to couple directly through, while simultaneously coupling the 1900nm signal light across. The cross-port of the pump-signal combiner has an integrated Si_3N_4-based grating, which serves both as a laser resonator-forming reflecting element and as a dispersion-compensating component (Section 3.4). The laser cavity is formed by the integrated grating on one end, an NLI on the other end, and three gain sections in between, connected with compact bends. The unique design of the bends together with the parameters of the gain waveguide allows for the compact footprint of this laser.

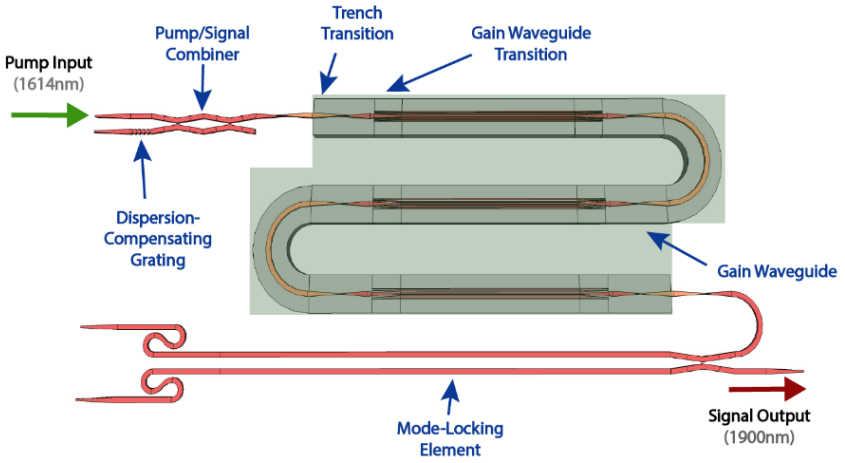

Fig. 1. Schematic of the MLL architecture (not to scale).

All the lasers and test structures described in this work, with the exception of the rare-earth-based gain material, were fabricated at Colleges of Nanoscale Science and Engineering (CNSE) at SUNY Polytechnic Institute in Albany, New York, on a 65nm CMOS 300mm wafer platform. The laser gain material used for 1900nm emission was deposited over individually diced chiplets at MIT's Microsystems Technology Laboratories.

The photonic layers for the full fabrication process are shown in Fig. 2. Starting from SOI wafers, photonic layers include three Si_3N_4 layers, with 400nm, 200nm, and 200nm respective thicknesses. We refer to those layers, from the 400nm layer up, as "BN" for "Bottom Nitride", "FN" for "First Nitride", and "SN" for "Second Nitride". The top two Si_3N_4 layers are separated by 100nm, allowing for the design of the waveguides where the optical mode at 1900nm will reside in both 200nm Si_3N_4 layers simultaneously. A large 4μm-deep photonic trench is etched in SiO_2 over the gain region of the lasers, with the "SN" Si_3N_4 layer serving

Optics EXPRESS

as the etch stop. The gain material (thulium-doped aluminum oxide glass), deposited on top of the chip, partially fills in the trench to a thickness of 1.1µm.

To characterize the optical properties of the photonic layer materials, separate films of Si_3N_4 were deposited and the refractive indices were measured using the prism-coupler technique at multiple wavelengths for each nitride layer. Index-vs-wavelength data were fit to the Sellmeier formula which in turn was used in the photonic design process. Linear losses of each silicon nitride layer were measured for each wafer by using ring-resonator test-structures implemented in corresponding layers [26].

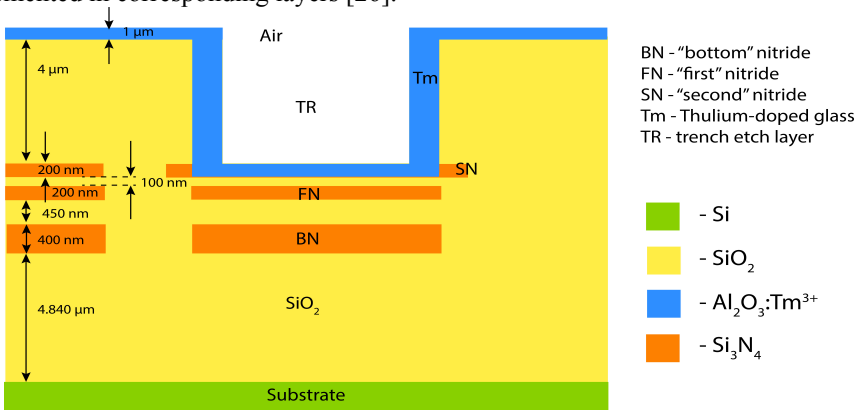

Fig. 2. Photonic layers used in fabrication process.

Due to various design requirements (such as loss, effective Kerr nonlinearity, and dispersion), different MLL components are implemented using different available photonic layers from Fig. 2. Layer-to-layer transition components are designed to facilitate low loss light coupling between those layers. Table 1 lists the main MLL photonic components and the corresponding fabrication layers they are implemented in.

Table 1. MLL components and corresponding photonic layers.

Component Name	Layer Name	Layer Height [nm]
Input/Output spotsize converters	FN/SiO_2/SN	200/100/200
Pump/Signal combiner	BN	400
Gain waveguide	FN/SiO_2/Tm	200/100/1100
Compact bends (connecting gain waveguide sections)	BN	400
Mode-locking element	FN/SiO_2/SN	200/100/200
Chirped grating	BN	400

3. Laser components design and characterization

3.1 Pump/signal combiner

The purpose of the pump/signal combiner element is to allow the 1600nm pump light to enter the gain waveguide and to simultaneously guide the 1900nm light coming from the MLL to the chirped grating that serves as the end-reflector of the laser. This component was designed as a Mach-Zehnder interferometer with zero phase delay for 1900nm which consists of two directional couplers, each having 50% transmission at 1900nm. The layout of the pump/signal combiner is shown in Fig. 3(a), with a close-up of a single directional coupler shown as close-up underneath the layout.

Optics EXPRESS

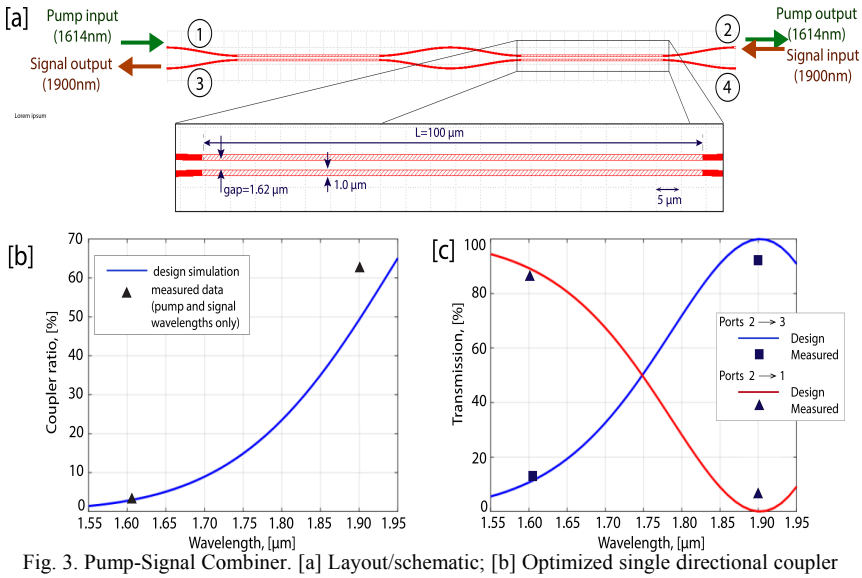

Fig. 3. Pump-Signal Combiner. [a] Layout/schematic; [b] Optimized single directional coupler performance vs wavelength; [c] Transmission of the final MZI device with two directional couplers.

The device was designed in a BN nitride layer. The width of the waveguide was chosen to be 1.0µm to allow for single-mode propagation of both the pump and the signal wavelengths. The length and the gap of the directional couplers were optimized in order to achieve the desired 50% transmission at 1900nm for each coupler, while simultaneously minimizing cross-coupling at 1600nm. The optimized directional coupler splitting ratio vs wavelength is shown in Fig. 3(b). The final optimized Mach-Zehnder device transmission vs wavelength is shown in Fig. 3(c). The optimized pump design transmission through the device is 89%, while the signal transmission across the device is 100%.

The devices were characterized using a variation of the cut-back method, where multiple identical directional couplers were nested together in a branch-tree configuration, allowing accurate measurements of the through- and cross-coupling for both wavelengths. On/off chip coupling losses and transition component losses were calibrated out. The final measured device insertion loss for the 1600nm pump coupling through the device (port 1 → port 2) is 0.6dB, which allows 86% of the pump to pass through the device. The loss for the 1900nm signal coupling across the device (port 2 → port 3) is 0.35dB, which results in 92.5% of the signal coupling across the device. The discrepancy between measured and simulated values for the device transmission are most likely due to fabrication-induced variances of device dimensions.

3.2 Gain material and gain waveguide

The gain material used for 1900nm emission is thulium-doped aluminum oxide glass (Al_2O_3:Tm^{3+}), which is deposited over the individual diced chiplets. Aluminum oxide glass has been shown to be a low loss host for various rare earth dopants [27,19], while thulium provides optical gain and lasing at 1900nm due to its $^3H_6$-$^3F_4$ atomic transition [28]. The gain film is deposited using RF magnetron co-sputtering of aluminum and thulium with argon plasma and a controlled O_2 rate, under high vacuum and at a substrate temperature of 415°C. Two widely used thulium pumping schemes for 1900nm emission are the in-band pumping of the $^3H_6$-$^3F_4$ transition with 1600nm light and the out-of-band pumping of the $^3H_6$-$^3H_4$ transition with 790nm. While the 790nm pumping scheme is quantum-mechanically more efficient due to the cross-relaxation process which generates two 1900nm photons for each absorbed 790nm photon, the 1600nm pumping scheme significantly simplifies the photonic

Optics EXPRESS

design of the MLL. Many MLL components (gain waveguide, bends, photonic layer transitions) must work for both the pump and the signal simultaneously, which is significantly easier to achieve when the pump and the signal wavelengths are close to each other. Therefore, MLLs in this work were designed for 1600nm pumping.

Al_2O_3:Tm^{3+} films were characterized spectroscopically to obtain the upper-state lifetime, absorption cross-sections, background losses, and active ion concentration [29]. These parameters were subsequently fed into a comprehensive laser gain model that was used to design the gain waveguide cross-section and to optimize the length of individual gain sections. Separate gain films with various thicknesses and active ion concentrations were deposited on SOI wafers to be used for spectroscopic characterization. In order to achieve different active ion concentrations, different levels of RF power were applied to thulium targets in the deposition chamber. The Rutherford back-scattering technique was used on each of those films to measure the active ion concentration. Absorption cross-section was extracted from the loss measurements on active films using a Metricon 2010/M prism coupler as a function of wavelength (for both 790nm and 1600nm) using the known active ion concentration values. Film background losses were measured with a prism coupler at 633nm, which is outside of absorption/emission of thulium, and were used as upper bound values. Upper state lifetimes were measured by characterizing the amplitude and phase response of a 1900nm signal coupled through the waveguide with a large mode fraction in the gain material, as a function of the frequency and amplitude of the modulated 1600nm pump light [29]. A summary of the relevant spectroscopic parameters is given in Table 2.

Table 2. Spectroscopic parameters of Al_2O_3:Tm^{3+} films.

Upper state spontaneous emission lifetime, τ_u	568 ± 48 µs
Absorption cross-section (at 1614nm), σ_a	2.75×10^{-21} cm^2
Absorption cross-section (at 790nm), σ_a	6.5×10^{-21} cm^2
Film background losses, α_b	0.1 dB/cm
Thulium ion concentration*, N_t	2.9×10^{20} cm^{-3}

*Thulium ion concentration is given for the actual film used in final demonstrated MLLs

The cross-section of the gain waveguide is shown schematically in Fig. 4(a). It consists of a 5-piece, 200nm thick segmented silicon nitride waveguide, a 100nm oxide gap layer, and a 1.1µm thick layer of Al_2O_3:Tm^{3+}. A 4µm-deep trench is etched into the SiO_2 layer, over the entire active area of the chip to allow the gain material to be within 100nm of the Si_3N_4 layer. The pump and signal modes are guided by the silicon nitride pieces, but the majority of the optical modes reside in the thulium-doped aluminum oxide layer. The waveguide was designed to optimize the overlap of the pump and signal modes with each other and with gain material, and to ensure sufficient pump intensity in the gain material to invert the population of active ions. The Si_3N_4 waveguide design was chosen to be segmented because this reduces the effective index of the signal and pump modes, and thus increases the mode fraction inside the gain region. The optimized gain waveguide has a 60% pump-signal overlap in the gain material. The pump and the signal intensity modes are shown in Fig. 4(b) and 4(d) respectively. The mode confinement factor in the gain material is 83% for the 1614nm pump, and 79% for the 1900nm signal for the optimized gain film thickness of 1.1µm.

Optics EXPRESS

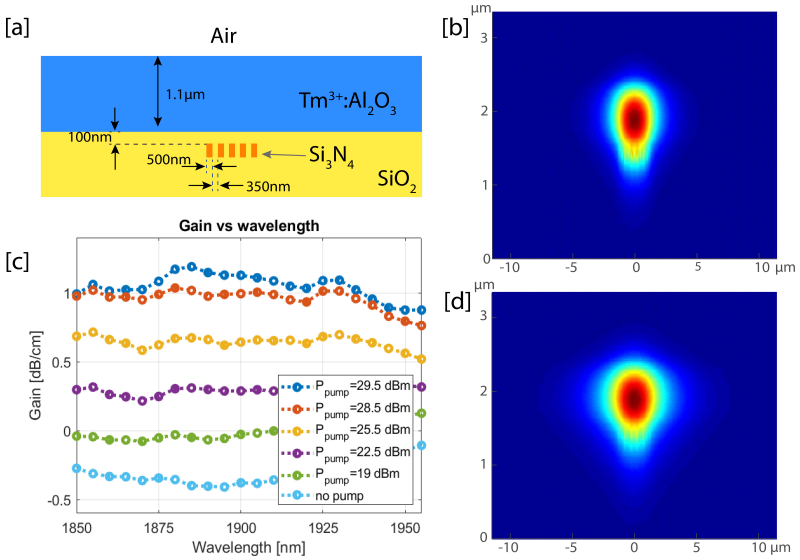

Fig. 4. [a] Gain waveguide schematic; [b] Optical intensity profile of the gain waveguide for the pump (1614nm) mode; [c] Measured gain spectrum; [d] Optical intensity profile of the gain waveguide for the signal (1900nm) mode.

To measure the small-signal gain of the gain waveguide described above, a separate gain test structure was added to each chip. This test structure included three sections of the gain waveguide interconnected with compact bends as shown in Fig. 1, but with pump/signal combiners at the input and output of the chip and no mode-locking or dispersion-compensating elements. The pump and a low level of signal were coupled into the gain waveguide and the output signal enhancement was measured as a function of pump power. The insertion losses of the pump/signal combiners, transition elements, and on/off chip coupling losses were calibrated out. The results of the gain measurement are shown in Fig. 4(c).

3.3 Compact bends

Compact bends at the end of the gain waveguide sections were designed to bend both the pump and the signal light by 180 degrees. In order to minimize the bend radius, prior to the bend the optical mode is shifted from the main gain waveguide to the bottom silicon nitride layer by an adiabatic taper transition. First, the segmented FN layer Si_3N_4 pieces composing the gain waveguide of Fig. 4(a) are tapered to form a single, wider Si_3N_4 piece, which is shown in Fig. 5(a). This is done by slowly moving the four nitride side blocks away from the central one, while increasing the width of the central nitride piece. Next, the width of this central FN layer piece is slowly decreased while the width of the bottom 400nm thick BN layer is slowly increased. The higher effective index of the BN layer pulls the optical mode down until it is mostly confined in that layer, as shown in Fig. 5(b). Insertion loss for this transition component was measured by a variation of the cut-back method, where 20, 30 and 40 such transitions were nested together back-to-back. Measured loss per each such transition is 0.02 dB at 1900nm.

Optics EXPRESS

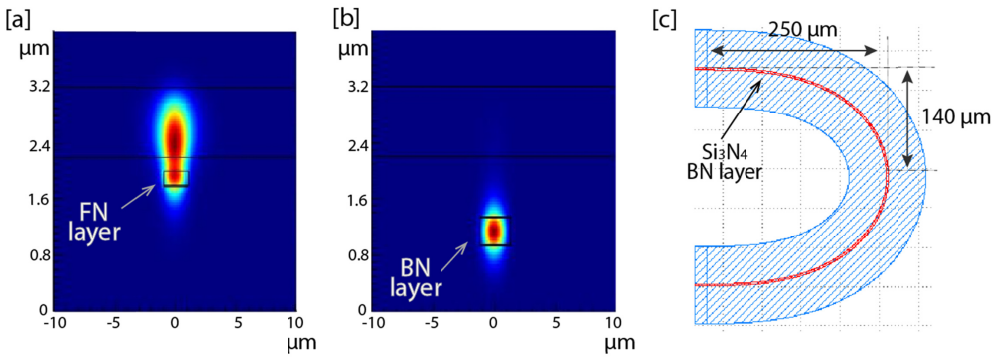

Fig. 5. Intensity of the optical mode at the beginning [a] and the end [b] of the vertical layer transition; [c] Compact bend layout.

Once the light is in the bottom nitride layer, a 180° compact bend is implemented (Fig. 5(c)). The bend design, based on the Euler spiral, has a radius of curvature that increases linearly as a function of the path length, so that $1/R = d\theta/ds$, where R is the bend curvature, θ is the angle, and s is the path length [30]. Such a smooth change in bend curvature eliminates abrupt transitions from straight to bend mode typically responsible for bend losses. The waveguide cross-section for the Euler bend in the BN layer is 400 × 2500nm, and the smallest bend radius at the 90° point of the bend is 60μm. Per-bend losses were measured to be under 0.04dB for both the pump and the signal wavelengths. Four bends per cavity roundtrip result in the accumulated insertion loss of only about 0.16dB.

3.4 Dispersion-compensating grating

One of the two reflectors forming the laser resonator cavity is an integrated grating implemented in silicon nitride. The grating serves both as a reflecting element for the 1900nm signal and as a dispersion-compensating element in the laser cavity. For soliton-based mode-locking, net MLL dispersion should be slightly anomalous in order to achieve the shortest pulses [31–33]. The dispersion of most of the MLL components is normal (Section 4); therefore, the anomalous dispersion of the grating is carefully designed to over compensate for the net normal dispersion in the rest of the laser. Section 4 describes the modeling of the mode-locking dynamics based on the optimum anomalous dispersion value of the grating.

The key design parameters for the grating are the 1900nm central wavelength, over 30nm of bandwidth to support optical pulses shorter than 100fs, high (over 95%) reflectivity across this bandwidth, and targeted amount of anomalous dispersion.

This integrated chirped grating is implemented in the BN layer since the 400nm Si_3N_4 thickness allows for a larger refractive index contrast, resulting in a stronger grating with larger anomalous dispersion. The perturbation of the refractive index forming the grating is achieved by adding small side blocks to the main 900nm-wide Si_3N_4 waveguide as shown schematically in Fig. 6(a). The side blocks are 1.6μm wide. The wavelength chirp is introduced by changing the length of the individual side blocks, keeping the main waveguide width constant. A third order polynomial function was used to obtain the grating period necessary to achieve the desired group-delay-dispersion. The grating has a symmetric apodization profile which aids in reducing group-delay oscillations typical in chirped mirrors and allows the grating to be broadband. Figure 6(d) shows the simulated apodization profile of the grating as a function of normalized position within the device. Simulated reflectivity and group delay dispersion (GDD) are shown in Fig. 6(b) and 6(c), for three different grating designs with group delay dispersion values of $-46{,}000fs^2$, $-38{,}000fs^2$, and $-30{,}000fs^2$. All three gratings have a relatively ripple-free GDD profile over 100nm, centered at 1900nm. The two gratings with highest anomalous dispersion values have reflection above 95% across

Optics EXPRESS

100nm, and the grating with −30,000fs^2 has reflection over 90% across the same wavelength range. Larger anomalous GDD values result from longer gratings, which also provide stronger reflection (smaller insertion loss); therefore, there is a fundamental trade-off between the amount of anomalous dispersion and insertion loss. All three designed gratings have dispersion values which put the net dispersion of the MLL into the anomalous regime and provide more-than-sufficient bandwidth to support pulse durations of under 50fs.

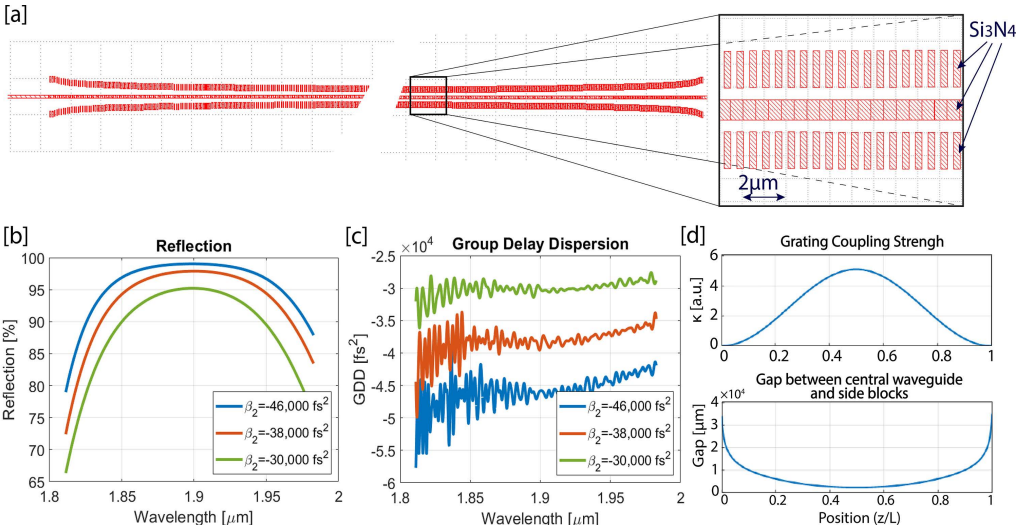

Fig. 6. [a] Chirped grating layout; [b] Reflection profile for three designs; [c] Corresponding GDD profiles for three different designs; [d] top – grating coupling strength as a function of normalized position, bottom – gap between central waveguide and side blocks, as a function of normalized position along the grating.

3.5 On-chip mode-locking element

The mode-locking element in the laser is an integrated nonlinear interferometer device, which is based on the Kerr nonlinearity of silicon nitride [18,34]. The schematic of the device is shown in Fig. 7(a). The device has an input coupler with a 90/10 splitting ratio at 1900nm between its two arms. Each arm consists of a 9.8mm long section of Si_3N_4 waveguide and is terminated with a near-perfect reflector, implemented as an integrated loop mirror. The loop mirrors reflect 99.8% of the incident light back into the interferometer arms and the light is recombined at the coupler. At low power the 90% output of the device goes back into the laser while the 10% port is used as the MLL output. The two arms of the interferometer have identical lengths, cross-sections, and loop mirrors. Therefore, at low incident power the nonlinear interferometer acts as a CW reflector forming the right side of the laser resonator cavity. At higher incident power a differential nonlinear phase shift forms between the two arms of the device due to the difference in their powers and Kerr nonlinearity. This nonlinear phase shift is proportional to the effective nonlinearity of the waveguide, the length of the waveguide, and the power difference between the two arms. The output of the nonlinear interferometer in this case has a sinusoidal-like dependence on the input power that, with proper linear bias, can provide higher reflection for higher incident power and act as a fast artificial saturable absorber.

To ensure the proper linear phase bias, integrated titanium-gold micro-heaters were deposited along the two arms after the gain medium deposition. The heaters are 20μm wide, 8mm long, with a thickness of 150nm of titanium followed by 100nm of gold. The average resistance of a heater is 180 Ohms. By applying current to one heater, linear phase bias is introduced to a corresponding device arm due to thermo-optic coefficient of silicon nitride.

Optics EXPRESS

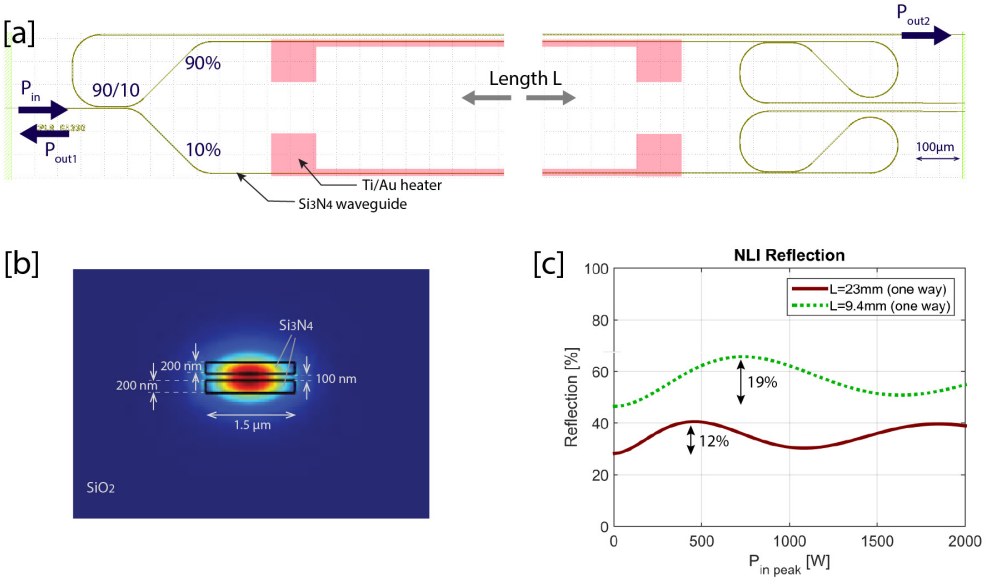

Fig. 7. Integrated mode-locking element. [a] Overall schematic/layout of the device; [b] waveguide cross-section with electric field intensity profile; [c] Nonlinear reflection for two different device lengths.

This device is implemented with a combination of the FN and SN silicon nitride layers, which allows a waveguide cross-section with maximized effective nonlinearity and minimized dispersion. The cross-section of the optimized waveguide, along with the optical mode, are shown in Fig. 7(b). Longer interferometer lengths allow the accumulation of higher Kerr nonlinearity but also decrease the reflected power due to accumulated linear losses of the silicon nitride waveguide. Lower power at the output of the interferometer results in significantly reduced CW laser power in the cavity. Therefore, the device length is optimized to provide sufficient reflection back into MLL cavity, while also providing a sufficiently large self-amplitude-modulation coefficient (the slope of reflection vs peak power) and modulation depth for the expected incident power during laser operation. Simulated transmission and reflection of the device are shown in Fig. 7(c) for two different device lengths – 23mm and 9.8mm (one-way length). For 23mm-long devices the simulated modulation depth is 12.3% and self-amplitude-modulation coefficient is 3.7×10^{-4} W^{-1}. For 9.8mm-long devices, the modulation depth is 19.2% and the self-amplitude-modulation coefficient is 2.8×10^{-4} W^{-1}. The 23mm devices were characterized as separate nonlinear interferometer test structures using femtosecond optical pulses from a commercial optical parametric oscillator centered at 1900nm. The measured modulation depth of the device was 9% (compared with the theoretical value of 12%), and the self-amplitude-modulation coefficient extracted from measured data was 7×10^{-5} W^{-1} [16]. The discrepancy between the design and the measured values are likely due to underestimating the waveguide dispersion. Higher normal dispersion will result in greater pulse spreading inside of the nonlinear interferometer, thereby decreasing the peak pulse power and reducing both the effective self-amplitude-modulation coefficient and modulation depth.

4. Laser mode-locking dynamics

We investigate the steady-state mode-locking characteristics of the laser by using a Nonlinear Schrodinger Equation (NLSE)-based model of the complete MLL. For each integrated photonics sub-component in the MLL cavity, the parameters such as gain/loss, Kerr

Optics EXPRESS

nonlinearity, dispersion, and effective mode area, are measured and calculated. Those parameters are then put into an NLSE model based on the following equation:

$$\frac{\partial A(z,t)}{\partial z} = \frac{\beta_2}{2}\frac{\partial^2 A(z,t)}{\partial t^2} - j\gamma_{NL} \mid A(z,t\mid^2\ A(z,t) + gA(z,t) - lA(z,t) \qquad (1)$$

where $A(z,t)$ is field amplitude, defined such that $|A(z,t)|^2$ is the optical power, β_2 is the dispersion in fs^2/m, γ_{NL} is the effective nonlinearity in $(W\text{-}m)^{-1}$, l is the linear loss in units of m^{-1}, g is the energy-dependent electric field gain in units of m^{-1}, where power gain is defined as $g = g_0/(1 + E_{sat}/E)$, where E is pulse energy at any given time and g_0 is small signal gain. Table 3 lists all the MLL components used in the model, with their respective parameters. The NLSE is numerically solved in a slowly-varying envelope approximation for each successive MLL component. The result of a stable and well-designed MLL is a steady-state pulse which circulates inside the laser cavity. It should be noted that this analysis does not take into account the laser start-up or laser gain dynamics that would have to be included to describe Q-switching behavior.

Table 3. Dispersion and nonlinearity values for MLL components, in order of appearance in MLL cavity.

	Layer	Width	Length	Component dispersion	Component nonlinearity	Round-trip dispersion	Round-trip nonlinearity
		µm	mm	fs^2/mm	$(W\ m)^{-1}$	fs^2	W^{-1}
Chirped grating	BN	0.7		-		−38,000	
Pump/Signal combiner	BN	1.0	0.430	2001	0.78	1,721	6.7×10^{-4}
Gain waveguide (part 1)	FN/TR	-	20.03	100	0.088	4006	3.5×10^{-3}
Euler bend 1	BN	2.5	0.6	761	0.7	913	8.4×10^{-4}
Gain waveguide (part 2)	FN/TR	-	19.7	100	0.088	3,950	3.5×10^{-3}
Euler bend 2	BN	2.5	0.6	761	0.7	913	8.4×10^{-4}
Gain waveguide (part 3)	FN/TR	-	20.03	100	0.088	4006	3.5×10^{-3}
BN waveguide	BN	1.0	0.26	2001	0.78	1035	4.0×10^{-4}
NLI	FN/SN	1.50	9.48	820	0.6	15,547	1.1×10^{-2}
					Total:	**-5,910**	

The flow of the model is shown in Fig. 8(a), with components in order of appearance in the MLL cavity (from Fig. 1), starting from the chirped grating side. The model includes the chirped grating, pump/signal combiner, three near-straight sections of gain waveguide with connecting bends, a small section of BN waveguide connecting the last section of gain waveguide to the NLI, and the NLI itself. The dispersion of the chirped grating used for this model is $-38{,}000fs^2$, which makes the net dispersion of the laser $-5{,}910fs^2$ - in the net anomalous regime as shown in Table 3. The NLSE model for this laser converges on a steady state solution. The resulting pulse duration dynamics as a function of position along the laser cavity are shown in Fig. 8(b). Since most of the components in the laser have normal dispersion, the pulse is up-chirped when it is incident on the grating. The grating provides a large amount of anomalous dispersion which over-compensates for the normal dispersion of the rest of the cavity. The pulse exits the grating strongly down-chirped, and as it propagates through the gain material towards the NLI the normal dispersion of the gain waveguide slowly counteracts the negative chirp, shortening the pulse as it propagates towards the NLI. Compact bends, although short compared with the gain waveguide, have a larger amount of normal dispersion per unit length, and this is evident in the sudden slope changes on the pulse duration plot in places that coincide with bend locations. The NLI provides a large amount of normal dispersion, and the pulse is again up-chirped as it exits the nonlinear interferometer. The pulse duration changes by over 100fs as it circulates within the laser, with pulse duration being the shortest when the pulse is incident on the NLI, and longest when the pulse is incident on chirped grating. The output of the MLL is directly after the NLI – not quite at the point of shortest pulse duration. This suggests that a better MLL design should have more

Optics EXPRESS

uniform dispersion distribution within the laser cavity. Future designs include redistributing the anomalous dispersion by placing gratings at both ends of the MLL cavity - within NLI itself as well as after the pump-signal combiner. This way the pulse duration will be more constant within the laser and the output of the NLI could be designed to have the shortest duration.

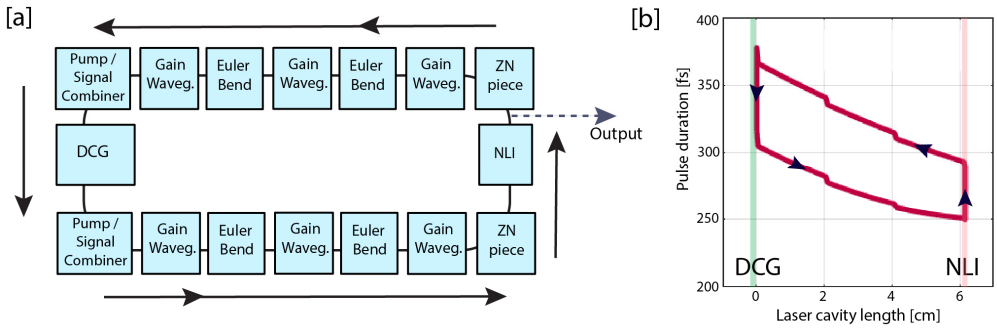

Fig. 8. [a] Nonlinear Schrodinger Equation cavity simulation flow. [b] The result of the NLSE laser model - a steady state pulse duration evolution for one cavity roundtrip. DCG – dispersion-compensating grating, NLI – nonlinear interferometer, ZN – "zero nitride" waveguide section.

5. Results

The lasers were characterized using a setup shown in Fig. 9(a). The pump laser was an L-band EDFA, seeded with a tunable laser at 1614nm. The pump was delivered to the chip through a fiber-based polarization controller and a lensed SMF28 fiber with a 3µm spot size at 1550nm wavelength. The signal from MLL was collected using SM2000 fiber with a lensed tip with a spot size of 3µm at 2µm wavelength. The output was split between two paths, with one path being directed into an optical spectrum analyzer (OSA), and another part going into the fast photodetector (12.5GHz electrical bandwidth) that was connected to an oscilloscope and an RF spectrum analyzer. A photo of an individual chip is shown in Fig. 9(b). Each chip contains 9 full MLLs and numerous other test structures. Titanium/gold heaters, deposited on top of NLI arms, are visible on top of each MLL.

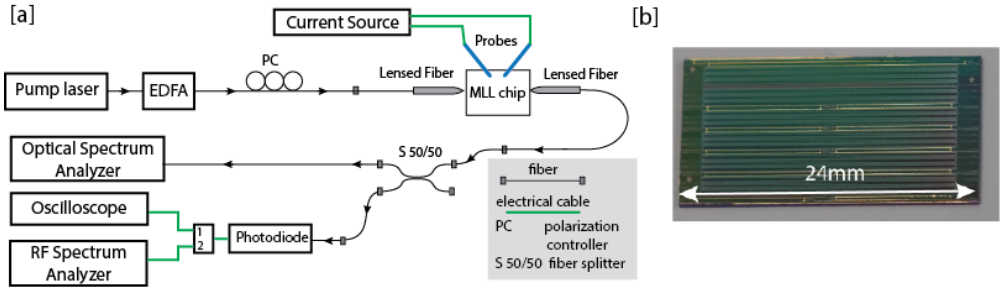

Fig. 9. [a] Characterization setup; [b] Photo of a chip with 9 MLLs.

Figure 10(a) shows the on-chip MLL power as a function of the pump power. CW lasing threshold occurs at around 45mW of pump power on-chip. At about 170mW of pump power, the lasers go into a Q-switched and mode-locked (QSML) regime. Maximum achieved on-chip outside-of-the-laser-cavity average MLL power is 9mW, which is limited by available pump power. Figure 10(b) shows the optical spectrum of the laser in the QSML regime. The central wavelength of the laser is around 1880nm, which is a result of both the emission spectrum of thulium and the wavelength-dependent losses in the laser cavity. The fit for a sech^2 pulse is overlaid on top of the spectrum, with a 17nm 3dB bandwidth which could

Optics EXPRESS

support pulses as short as 215fs. A few spikes on the optical spectrum indicate that during the sweep the laser is Q-switching as well as mode locking.

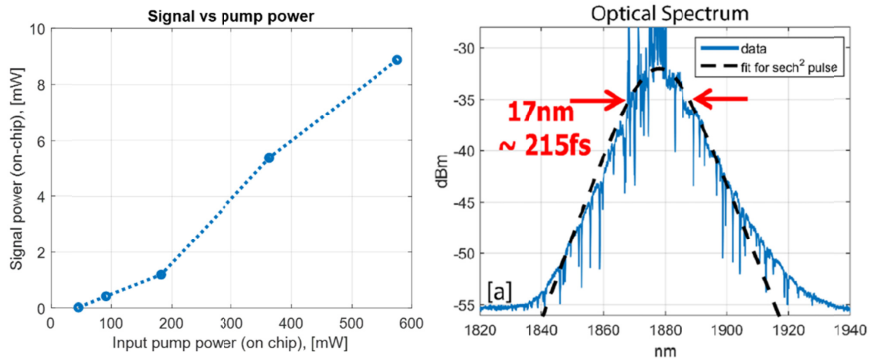

Fig. 10. [a] Signal power (on-chip) vs pump power (on-chip); [b] Optical spectrum.

Figure 11(a) shows the temporal periodicity of the Q-switching to be 720 kHz. The Q-switching rate changed with input pump power from 500kHz to about 1MHz. A close-up of one Q-switched pulse, in Fig. 11(c), shows individual mode-locked pulses underneath the envelope. A further close-up on individual pulses is shown in Fig. 11(d), indicating that individual mode-locked pulses are 0.8ns apart, which corresponds to cavity repetition rate of 1.2GHz. This repetition rate is also directly observed in the RF domain, shown in Fig. 11(b).

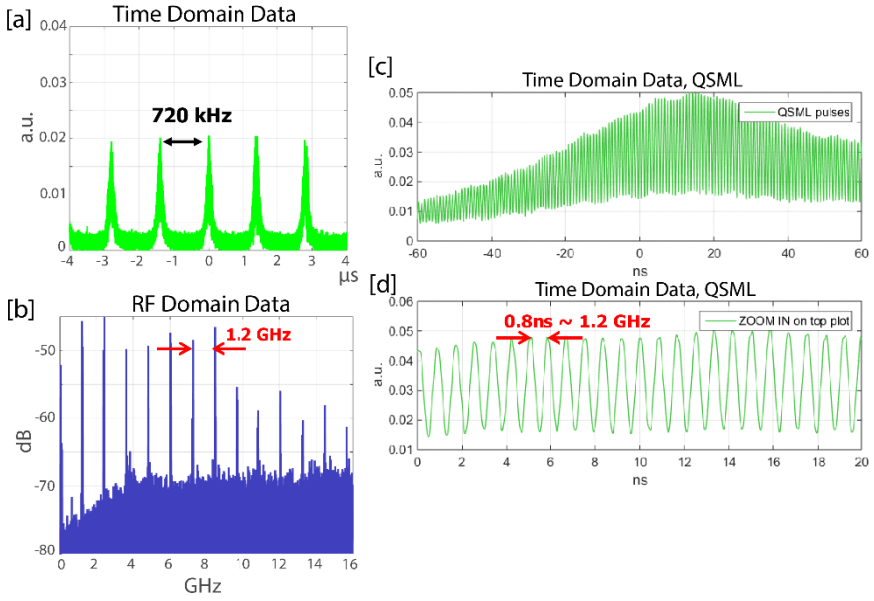

Fig. 11. MLL results: [a] Time-domain data showing Q-switching; [b] RF spectrum; [c] Time-domain data, close up of one Q-switched pulse; [d] Time-domain data, individual pulses.

Both Q-switching and mode-locking require proper biasing of the NLI. This is accomplished by selectively exciting the heater above one of the arms. Bias opposite to that which produces pulsing results in an increase in laser threshold and lower CW laser output.

Although Q-switching provides high peak power and high pulse energy, it is undesirable in frequency-comb-based applications. For future laser designs, modifications to suppress the Q-switching may include lower loss, increased net gain, higher net Kerr nonlinearity and perhaps a longer laser cavity [35].

Optics EXPRESS

6. Conclusion

In this work, we have demonstrated Q-switching and mode-locking in an integrated laser operating near 1900nm in a silicon nitride-on-insulator platform, with thulium-doped aluminum glass as a gain material. The laser is fabricated using a CMOS-compatible 300mm wafer platform, with the gain material deposited separately over SiN/SiO_2 layers. The laser, with a footprint of 23.6 × 0.6mm, is completely integrated on a chip, with no off-chip components with the exception of a 1614nm pump laser. Maximum on-chip signal power is 9mW, with the fundamental repetition rate of 1.2 GHz and Q-switching rate of 720kHz. The laser produces optical pulses centered at 1880nm, with 17nm optical bandwidth which is sufficient to support pulses as short as 215fs. This work is a major step towards all-integrated CMOS-compatible CW-mode-locked lasers. With suppression of Q-switching instabilities and on-chip pump integration, this laser architecture, together with electronic-photonic integration, could enable stabilized MLL-based on-chip frequency combs, low phase noise microwave sources, and high speed communications applications, fabricated with a compact footprint using CMOS and CMOS-compatible processes.

Funding

DARPA DODOS HR0011-15-C-0056, AFOSR FA9550-12-1-0499, DESY - a Center of Helmholtzf Association, NDSEG fellowship 32 CFR 168a.I, National Science Scholarship (NSS) from A*STAR Singapore.

References

1. T. Pfeiffer and G. Veith, “40 GHz pulse generation using a widely tunable all-polarization preserving erbium fibre ring laser,” Electron. Lett. **29**(21), 1849–1850 (1993).
2. E. Yoshida and M. Nakazawa, “80~200 GHz erbium doped fibre laser using a rational harmonic mode-locking technique,” Electron. Lett. **32**(15), 1370–1372 (1996).
3. E. Yoshida and M. Nakazawa, “Low-threshold 115-GHz continuous-wave modulational-instability erbium-doped fiber laser,” Opt. Lett. **22**(18), 1409–1411 (1997).
4. A. Pasquazi, M. Peccianti, B. E. Little, S. T. Chu, D. J. Moss, and R. Morandotti, “Stable, dual mode, high repetition rate mode-locked laser based on a microring resonator,” Opt. Express **20**(24), 27355–27362 (2012).
5. L. Krainer, R. Paschotta, J. Aus der Au, C. Hönninger, U. Keller, M. Moser, D. Kopf, and K. J. Weingarten, “Passively mode-locked Nd:YVO4 laser with up to 13 GHz repetition rate,” Appl. Phys. B **69**(3), 245–247 (1999).
6. L. Krainer, R. Paschotta, M. Moser, and U. Keller, “77 GHz soliton modelocked Nd:YVO4 laser,” Electron. Lett. **36**(22), 1846–1848 (2000).
7. U. Keller, “Recent developments in compact ultrafast lasers,” Nature **424**(6950), 831–838 (2003).
8. G. Chang, C. H. Li, D. F. Phillips, A. Szentgyorgyi, R. L. Walsworth, and F. X. Kärtner, “Optimization of filtering schemes for broadband astro-combs,” Opt. Express **20**(22), 24987–25013 (2012).
9. M. Y. Sander, S. Frolov, J. Shmulovich, E. P. Ippen, and F. X. Kärtner, “10 GHz femtosecond pulse interleaver in planar waveguide technology,” Opt. Express **20**(4), 4102–4113 (2012).
10. A. B. Grudinin and S. Gray, “Passive harmonic mode locking in soliton fiber lasers,” J. Opt. Soc. Am. B **14**(1), 144–154 (1997).
11. Y. K. Chen, M. C. Wu, T. Tanbun-Ek, R. A. Logan, and M. A. Chin, “Subpicosecond monolithic colliding-pulse mode-locked multiple quantum well lasers,” Appl. Phys. Lett. **58**(12), 1253–1255 (1991).
12. Y. K. Chen and M. C. Wu, “Monolithic Colliding-Pulse Mode-Locked Quantum-Well Lasers,” IEEE J. Quantum Electron. **28**(10), 2176–2185 (1992).
13. C. Sun, M. T. Wade, Y. Lee, J. S. Orcutt, L. Alloatti, M. S. Georgas, A. S. Waterman, J. M. Shainline, R. R. Avizienis, S. Lin, B. R. Moss, R. Kumar, F. Pavanello, A. H. Atabaki, H. M. Cook, A. J. Ou, J. C. Leu, Y. H. Chen, K. Asanović, R. J. Ram, M. A. Popović, and V. M. Stojanović, “Single-chip microprocessor that communicates directly using light,” Nature **528**(7583), 534–538 (2015).
14. C. McDonough, D. La Tulipe, D. Pascual, P. Tariello, J. Mucci, M. Smalley, A. Nguyen, T. Vo, C. Johnson, P. Nguyen, J. Hebding, G. Leake, M. Moresco, E. Timurdogan, V. Stojanović, M. R. Watts, and D. Coolbaugh, “Heterogeneous integration of a 300mm silicon photonics-CMOS wafer stack by direct oxide bonding and via-last 3D interconnection,” International Symposium on Microelectronics, 621–626 (2015).
15. R. Baets, A. Z. Subramanian, S. Clemmen, B. Kuyken, P. Bienstman, N. Le Thomas, G. Roelkens, D. Van Thourhout, P. Helin, and S. Severi, “Silicon Photonics: silicon nitride versus silicon-on-insulator,” in Optical Fiber Communication (OFC2016) Conference, paper Th3J.1.
16. D. J. Moss, R. Morandotti, A. L. Gaeta, and M. Lipson, “New CMOS-compatible platforms based on silicon nitride and Hydex for nonlinear optics,” Nat. Photonics **7**(8), 597–607 (2013).

Optics EXPRESS

17. P. C. Callahan, Purnawirman, T. N. Adam, G. Leake, D. Coolbaugh, M. R. Watts, and F. X. Kärtner, "Double-chirped Bragg gratings in a silicon nitride waveguides," in Lasers and Electro-Optics (CLEO2016), paper SF1E.7.
18. K. Shtyrkova, P. T. Callahan, M. R. Watts, E. P. Ippen, and F. X. Kärtner, "Integrated artificial saturable absorber based on Kerr nonlinearity in silicon nitride," in Lasers and Electro-Optics (CLEO2017), paper AF1B.6.
19. J. D. Bradley and M. Pollnau, "Erbium-doped integrated waveguide amplifiers and lasers," Laser Photonics Rev. **5**(3), 368–403 (2011).
20. E. S. Magden, N. Li, J. D. B. Purnawirman, J. D. B. Bradley, N. Singh, A. Ruocco, G. S. Petrich, G. Leake, D. D. Coolbaugh, E. P. Ippen, M. R. Watts, and L. A. Kolodziejski, "Monolithically-integrated distributed feedback laser compatible with CMOS processing," Opt. Express **25**(15), 18058–18065 (2017).
21. N. Li, P. Purnawirman, Z. Su, E. Salih Magden, P. T. Callahan, K. Shtyrkova, M. Xin, A. Ruocco, C. Baiocco, E. P. Ippen, F. X. Kärtner, J. D. Bradley, D. Vermeulen, and M. R. Watts, "High-power thulium lasers on a silicon photonics platform," Opt. Lett. **42**(6), 1181–1184 (2017).
22. N. Singh, M. Xin, D. Vermeulen, K. Shtyrkova, N. Li, P. T. Callahan, E. S. Magden, A. Ruocco, N. Fahrenkopf, C. Baiocco, B. P.-P. Kuo, S. Radic, E. Ippen, F. X. Kärtner, and M. R. Watts, "Octave-spanning coherent supercontinuum generation in silicon on insulator from 1.06um to beyond 2.4um," Light Sci. Appl. **7**(1), 17131 (2018).
23. E. Timurdogan, C. V. Poulton, M. J. Byrd, and M. R. Watts, "Electric field-induced second-order nonlinear optical effects in silicon waveguides," Nat. Photonics **11**(3), 200–206 (2017).
24. E. S. Magden, N. Li, M. Raval, C. V. Poulton, A. Ruocco, N. Singh, D. Vermeulen, E. P. Ippen, L. A. Kolodziejski, and M. R. Watts, "Transmissive silicon photonic dichroic filters with spectrally selective waveguides," Nat. Commun. **9**(1), 3009 (2018).
25. P. T. Callahan, K. Shtyrkova, N. Li, E. S. Magden, Purnawirman, C. Baiocco, D. Coolbaugh, E. P. Ippen, M. R. Watts, and F. X. Kärtner, "Fully-Integrated CMOS-compatible Q-Switched Laser at 1.9µm using thulium-doped Al2O3," in Lasers and Electro-Optics (CLEO2017), paper STh3N.
26. W. R. McKinnon, D. X. Xu, C. Storey, E. Post, A. Densmore, A. Delâge, P. Waldron, J. H. Schmid, and S. Janz, "Extracting coupling and loss coefficients from a ring resonator," Opt. Express **17**(21), 18971–18982 (2009).
27. K. Wörhoff, J. D. Bradley, L. Agazzi, and M. Pollnau, "Rare-earth-ion-doped Al2O3 for integrated optical amplification," in SPIE Proceedings, 7604 (2010).
28. J. Geng, J. Wu, S. Jiang, and J. Yu, "Efficient operation of diode-pumped single-frequency thulium-doped fiber lasers near 2 µm," Opt. Lett. **32**(4), 355–357 (2007).
29. E. Magden, P. Callahan, N. Li, J. Bradley, N. Singh, A. Ruocco, L. Kolodziejski, E. Ippen, and M. R. Watts, "Frequency domain spectroscopy in rare-earth-doped gain media," IEEE J. Quantum Electron. **24**(5), 1–10 (2018).
30. M. Cherchi, S. Ylinen, M. Harjanne, M. Kapulainen, and T. Aalto, "Dramatic size reduction of waveguide bends on a micron-scale silicon photonic platform," Opt. Express **21**(15), 17814–17823 (2013).
31. H. Haus, J. G. Fujimoto, and E. P. Ippen, "Structures for additive pulse mode locking," J. Opt. Soc. Am. B **8**(10), 2068–2076 (1991).
32. F. X. Kärtner, I. D. Jung, and U. Keller, "Soliton mode-locking with saturable absorbers," IEEE J. Quantum Electron. **2**(3), 540–556 (1996).
33. H. Haus, "Parameter ranges for cw passive modelocking," IEEE J. Quantum Electron. **12**(3), 169–176 (1976).
34. K. Shtyrkova, P. Callahan, N. Li, S. E. Magden, M. R. Watts, F. X. Kärtner, and E. P. Ippen, "Integrated CMOS-compatible Q-Switched-Mode-Locked Laser at 1.9µm with On-Chip Artificial Saturable Absorber," in Advanced Photonics 2018, paper IM3B.2.
35. C. Hönninger, R. Paschotta, F. Morier-Genoud, M. Moser, and U. Keller, "Q-switching stability limits of continuous-wave passive mode locking," J. Opt. Soc. Am. B **16**(1), 46–56 (1999).